John von Neumann Institute for Computing

Chemically Realistic Computer Simulations of Polymer Melts: Equilibration Issues and Study of Relaxation Processes

Wolfgang Paul

published in

Computational Soft Matter: From Synthetic Polymers to Proteins, Lecture Notes,
Norbert Attig, Kurt Binder, Helmut Grubmüller, Kurt Kremer (Eds.),
John von Neumann Institute for Computing, Jülich,
NIC Series, Vol. **23***, ISBN 3-00-012641-4, pp. 169-194, 2004.*

http://www.fz-juelich.de/nic-series/volume23

Chemically Realistic Computer Simulations of Polymer Melts: Equilibration Issues and Study of Relaxation Processes

W. Paul

Institut für Physik, Johannes Gutenberg-Universität,
55099 Mainz, Germany
E-mail: wolfgang.paul@uni-mainz.de

Introduction

Polymers are complex objects displaying non-trivial structure from the scale of a (typically) carbon-carbon bond (1 Å) to the radius of gyration of the coil ($R_g \approx 10 - 100$ Å[1]). Here we will be concerned with melts of simple linear polymers where the polymer coils behave as if they were random walks ($R_G \propto N$ where N is the degree of polymerization of the chains). Connected with the spread in length scales is an even wider spread in time scales: from local bond-length and bond-angle vibrations ($10^{-15} - 10^{-13}$ s) over conformational transitions between isomeric states in the dihedral potential ($10^{-12} - 10^{-10}$ s) to the self-diffusion and overall configurational relaxation of the whole chain which for short chains scales as N^2 times the time-scale for conformational transitions and for long chains as $N^{3.4}$ times that time-scale. With N ranging from 100 (short chains) up to 10000 and more (long chains) these time scales cover 10^{-8} s up to 10 s.

The local dynamics is naturally strongly dependent on the exact chemical nature and structure of the polymer one studies. The large scale dynamics, however, is largely universal and is described with the Rouse model whereas for longer chains the tube model and reptation concept is employed to describe the chain dynamics[2] (see also the contribution of K. Kremer in this volume). It is easy to see that no single simulation method can capture the physics of polymer dynamics on all these length and time scales[3]. To study the large scale dynamics in polymer melts therefore, simulations of coarse-grained models - both Molecular Dynamics (MD) and Monte Carlo (MC) methods were used - have been successfully applied. On large length and time scales entropy dominates the physical behavior of polymer melts giving rise to universality and therefore every model of a linear polymer faithfully representing excluded volume between monomers as well as connectivity of the chains can be used in computer simulation studies.

On the local scale, however, the detailed chemistry and energetics dominates structure as well as relaxation behavior. For situations where we can ignore quantum effects (which can, however, be important in polymer crystals[4]) MD simulations of chemically realistic force fields are the method of choice to study local relaxation.

Besides the necessity for carefully optimized chemically realistic force fields there is always the question to address whether the simulation is able to equilibrate the model system at a given thermodynamic state point of temperature, density and chain length. This means that the simulations mostly are limited to polymer melts well above the glass transition temperature (or density) and to chains not exceeding the entanglement molecular

weight.

In the next section we will introduce a simple chemically realistic force field for 1,4-polybutadiene (PB) which we will use as our model system for the discussions in this contribution. As this polymer is structurally simple and since there are no relevant partial charges or specific interactions present in this polymer melt, this polymer can be quantitatively described by a relatively simple force field and efficiently simulated using MD algorithms.

In section 2 we will then discuss the question of equilibration of such a system and methods developed for efficient equilibration in a computer simulation. Section 3 will then introduce some techniques for studying local relaxation processes in polymer melts and describe how to implement these measurements in a computer simulation. From there we will go in section 4 to the large scale dynamics in polymer melts as observable in chemically realistic simulations and will finish with some conclusions in section 5.

1 A Simple Chemically Realistic Force Field for PB

Chemically realistic force fields for polymers in general have a complicated functional form

$$\begin{aligned} H(\{\boldsymbol{r}_i\}) = & \sum_i U(l_i) + \sum_j U(\vartheta_j) + \sum_k U(\phi_k) \\ & + \frac{1}{2}\sum_{i,j} U_{\mathrm{disp}}(r_{ij}) + \frac{1}{2}\sum_{i,j} U_{\mathrm{Coul}}(r_{ij}) + U_{\mathrm{Hbond}} \\ & + \text{cross terms between all intramolecular potentials} + \ldots \end{aligned} \tag{1}$$

The first line contains the intramolecular potentials for bond lengths (harmonic), bond angles (harmonic) and dihedral angles, the second line contains the non-bonded interactions due to dispersion forces, Coulomb interactions and hydrogen bonds and the third line contains possible cross terms between all the intramolecular degrees of freedom. There are force fields in the literature containing easily over 30 parameters, able to fit about the same amount of experimental information.

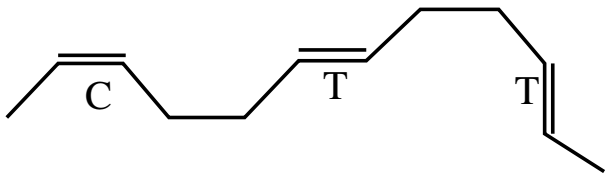

Figure 1. Schematic representation of the chemical micro structure of PB indicating two types of repeat units, cis and trans conformers.

To really understand the necessary ingredients of such a force-field, for instance to be able to reproduce experiments on polymer melts, one best starts with very simple polymers like polyethylene[5–9], polyisoprene[10,11], polyisobutylene[12] or polybutadiene[13], to give just a few selected examples. In the following we will focus on the force field used for PB[13],

see Fig.1 for a schematic representation of the chemical micro structure of the chains. Since we are not interested in very high frequency vibrational motion, we will first of all collapse the hydrogen atoms onto the carbons they are bound to, defining a united atom model, and furthermore constrain the carbon-carbon bonds to their mechanical equilibrium values. The non-bonded interactions for this polymer contain no Coulomb contribution and no hydrogen bonding (making a united atom approach possible). The force-field we are employing therefore has the form

$$H(\{\boldsymbol{r}_i\}) = \sum_j k_j^{\vartheta}(\cos(\vartheta_j) - \cos(\vartheta_0))^2 + \sum_j \sum_{n=1}^{6} k_{jn}^{\phi}(1 - \cos(n\phi_j)) + \frac{1}{2}\sum_{i,j} \varepsilon_{\alpha\beta}\left[\left(\frac{\sigma_{\alpha\beta}}{r_{ij}}\right)^{12} - 2\left(\frac{\sigma_{\alpha\beta}}{r_{ij}}\right)^{6}\right] . \quad (2)$$

The constants k_j^{ϑ} and k_{jn}^{ϕ} depend on the type of bond or torsion angle, and $\varepsilon_{\alpha\beta}$ and $\sigma_{\alpha\beta}$ depend on the types of interacting united atom group (CH, CH_2 or CH_3).

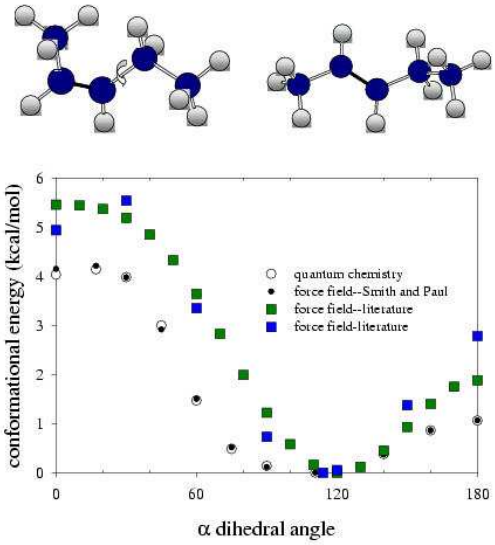

Figure 2. Effective potential (containing a non-bonded LJ contribution) for rotation around the alpha-bond next to the double bond (black bond in the cis-pentene molecule) in a cis group. The new force field is compared to literature force fields[14,15].

The parameters for the bond angle potential can be obtained from quantum chemistry and from spectroscopic information, for the accurate determination of the parameters of the dihedral potential, however, quantum chemistry is the only tool. Only quantum chemical calculations yield information on the barriers between different isomeric states in the dihedral potentials. This information is crucial for an accurate modeling of local conformational transitions between isomeric states, since their rate is exponentially sensitive to

the barriers[13]. And it is these transitions, as we will see in the following, which underly all local relaxation processes in a polymer melt and in general set the microscopic time scale (Rouse rate, effective segmental friction) for the large scale relaxation processes. Even more difficult to determine than the torsion force constants are the parameters of the dispersion forces. Equation of state and cohesive energy data are one source of experimental information these parameters can be gouged on, but much more sensitive are phase diagrams of small oligomers of the polymer under study[7].

These chemically realistic models can be simulated using MC as well as MD techniques. Advanced MC techniques which address the equilibration of these model systems will be discussed in the next section. When we want to study local relaxation processes we are bound to use MD simulation techniques which faithfully capture the short time ballistic and vibrational motion influenced by inertia effects. The quantitative reproduction of local relaxation processes needs a realistic dynamics on the fs to ns time scales. Typically one uses Verlet integrators in the NVE ensemble or their second order Runge Kutta counterpart when one switches to the NVT ensemble by using for instance a Nosé-Hoover thermostat. Although it can not be in general established that this change of ensemble has no influence on the relaxation behavior, it was empirically observed to have no discernible quantitative effect on the local relaxation behavior. The effectiveness of the MD code for these simulations can be increased using multiple time-step techniques[16].

2 Equilibration of Polymer Melts

In this section we want to address the question of equilibration of chemically realistic models of polymer melts. In addition to the methods discussed already in the contribution of K. Kremer on the study of reptation dynamics in polymer melts we will now discuss some advanced MC techniques developed for equilibration of dense polymer systems.

Basically, a discussion of the problems with the equilibration of polymer melt models can be divided into identifying the two main sources for slow relaxation in polymers, entanglement effects and the glass transition. The first one is entropic in origin, the second one - at least in chemically realistic polymer models - to a large degree enthalpic. We write the largest relaxation time in the melt as

$$\tau_1(T, N) = \tau_{\mathrm{mes}}(T) N^x \tag{3}$$

where τ_{mes} is a mesoscopic time scale. The chain length dependence crosses over from $x = 2$ for Rouse behavior to $x = 3.4$ for reptating chains. Every simulation method performing configuration changes typical for the mesoscopic time scale τ_{mes}, i.e., local rearrangements, leads to a relaxation of the large scale structure of the polymer chains in the melt only after O(N^x) such configuration changes, quickly limiting the range of chain lengths one can treat in thermodynamic equilibrium. To circumvent this problem one has to use advanced MC techniques implementing global configurational changes within a single Monte Carlo step.

A class of these advanced MC techniques is comprised of the so-called connectivity altering moves like the cooperative motion algorithm[17] on the lattice and the end-bridging algorithm[18,19] and its newest variant, the double-bridging algorithm[20]. The latter two have been developed with chemically realistic polymer models in mind and we will now shortly discuss the idea and properties of these algorithms.

In the original end-bridging algorithm[18,19] an end monomer i of one chain in the melt attacks a backbone atom j of another chain in sufficiently close proximity and tries to initiate a change in connectivity of the two involved chains by forming a trimer bridge to this backbone atom. In the event of a successful bridging the attacking chain grows by a part cut off the attacked chain and the attacked chain shrinks correspondingly. This description already exhibits the main drawbacks of the algorithm: it generates polydisperse polymer melts and it needs a sufficient amount of chain ends to be efficient. Empirically it was found that the efficiency of the algorithm dropped considerably as the stiffness of the chains was increased and in the presence of chain orientation. The fact that the algorithm generates polydisperse samples can be used to simulate the experimentally given molecular weight distribution through the so-called NpTμ^* ensemble where number of chains, number of monomers, pressure, temperature and the relative chemical potential of the different chain lengths are prescribed[18]. The latter thermodynamic constraints generate the desired molecular weight distribution. In this formulation the algorithm was successfully applied to, e.g., polyethylene melts[21] and cis-1,4 polyisoprene melts[10].

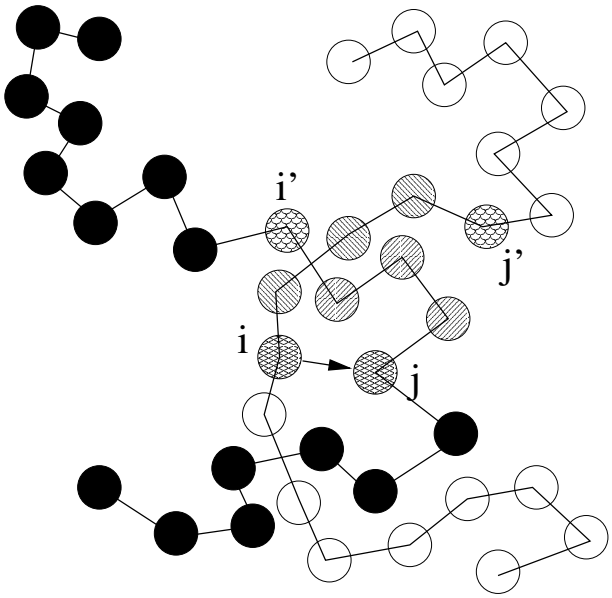

Figure 3. Monomer i of one chain attacks monomer j of a different chain. Only when the shaded trimers are cut off and bridges between i and j and i' and j' are formed, are the resulting chains of the same length as the original ones.

In the double-bridging algorithm an inner monomer of a chain attacks an inner monomer of another chain (or the same chain) and tries to form a trimer bridge (this is shown in Fig.3). Simultaneously another bridge is formed between two monomers which are 4 steps apart from the first two monomers along the two chains generating two new chains with exactly the same length as the original one. These requirements understandably put heavy geometric constraints on the configurations of the two chains for which

this type of move is feasible since only special choices of involved monomers (i, j) and excised trimers (on which side of i or j, respectively) conserve the chain lengths in the move. The trimer bridge itself is made of three monomers (atoms) connected by bonds of fixed lengths l making a fixed angle, which is chosen as the value at the maximum of the bond-angle distribution of the model. Whenever the monomers i and j have a distance less than the maximum bridgeable distance of $4l\cos((\pi - \theta_{\max})/2)$ this geometric problem is in principle solvable. Wu and Deem[22] have shown that it is equivalent to finding the solutions of an algebraic equation of order 16. Since each trimer bridging problem of the double-bridging algorithm therefore has between 0 and 16 solutions, the double bridging problem has between 0 and 256 solutions. To reduce this number Karayiannis et al.[20] suggest to discard directly solutions leading to a too high torsional energy or overlap between segments when hard spheres of diameter $\sigma = 3.2$Å are placed at the positions of the bridging atoms. From the remaining s energetically viable solutions, one is then chosen according to a Boltzmann factor involving the torsional and non-bonded energies

$$P_{\rm select}(\text{old} \rightarrow \text{new}) = \frac{\exp\{-\beta(V_{\rm tor}(\text{new}) + V_{\rm LJ}(\text{new}))\}}{\sum_{k=1}^{s_{\text{old}\rightarrow\text{new}}} \exp\{-\beta(V_{\rm tor}(k) + V_{\rm LJ}(k))\}} \; . \tag{4}$$

Here $\beta = 1/k_{\rm B}T$. The reverse move is selected according to

$$P_{\rm select}(\text{new} \rightarrow \text{old}) = \frac{\exp\{-\beta(V_{\rm tor}(\text{old}) + V_{\rm LJ}(\text{old}))\}}{\sum_{k'=1}^{s_{\text{new}\rightarrow\text{old}}} \exp\{-\beta(V_{\rm tor}(k') + V_{\rm LJ}(k'))\}} \; . \tag{5}$$

Furthermore, the selection of a given bridge site is done by choosing from a list of bridgeable sites from atom i, $N_{\rm DB}(i)$, which is constantly updated in the simulation.

$$\begin{aligned} W(\text{old} \rightarrow \text{new}) &= \frac{1}{[N_{\rm DB}(i)]_{\rm old}} \\ W(\text{new} \rightarrow \text{old}) &= \frac{1}{[N_{\rm DB}(j)]_{\rm new}} \; . \end{aligned} \tag{6}$$

The Metropolis acceptance criterion for the double-bridging move is therefore

$$\begin{aligned} &P_{\rm accept}(\text{old} \rightarrow \text{new}) = \\ &\min\left[1, \frac{W(\text{new} \rightarrow \text{old}) P_{\rm select}(\text{new} \rightarrow \text{old}) J(\text{new}) \exp\{-\beta V(\text{new})\}}{W(\text{old} \rightarrow \text{new}) P_{\rm select}(\text{old} \rightarrow \text{new}) J(\text{old}) \exp\{-\beta V(\text{old})\}}\right] \end{aligned} \tag{7}$$

where $J(\text{new})$ and $J(\text{old})$ are Jacobian determinants for the bridges degrees of freedom in the initial and final stage[20].

This algorithm was found to be especially efficient to relax the large scale conformation of the chains as observed typically through end-to-end vector decorrelation and center of mass diffusion. There are two at first glance counterintuitive observations connected with these relaxation functions in simulations with these connectivity changing algorithms: the center of mass of a chain diffuses faster than a single monomer and longer chains diffuse faster (have a faster end-to-end vector decorrelation) than shorter chains as is shown in Fig. 4. Both of them, however, can be understood by a simple random walk type argument as for instance presented in[23] or along slightly different lines in the following paragraph.

Consider for the double-bridging algorithm monomer $n, 3 \leq n \leq N/2 - 3$ attacking another chain successfully. The change in center of mass position of the chain n belongs

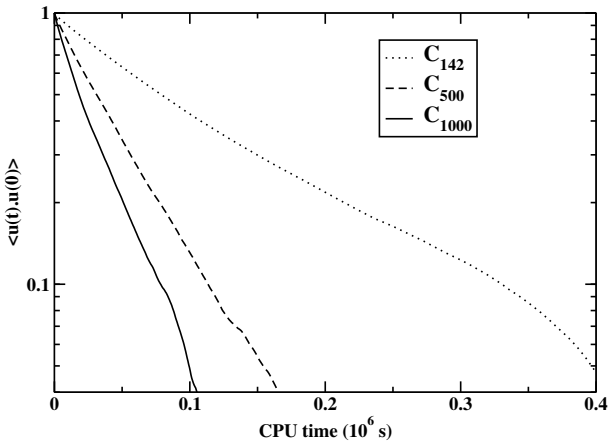

Figure 4. Autocorrelation function of the end-to-end unit vector for united atom model chains of alkanes of chain lengths $N = 142$ (dotted curve), $N = 500$ (dashed curve) and $N = 1000$ (full curve). One observes a clear decrease of the autocorrelation time scale with increasing chain length for the double-bridging algorithm. (I am grateful to the authors of[20] for supplying these data.)

to is given as

$$\Delta \boldsymbol{R}_{\mathrm{cm}} = \frac{1}{N} \sum_{i=n+1}^{N} (\boldsymbol{r}_i^{\mathrm{new}} - \boldsymbol{r}_i^{\mathrm{old}}) .$$

As $\boldsymbol{r}_i^{\mathrm{new}}$ and $\boldsymbol{r}_i^{\mathrm{old}}$ can be considered as random walks starting at the same position in space, we can write for the scaling of their difference

$$\Delta \boldsymbol{r}_i = \boldsymbol{r}_i^{\mathrm{new}} - \boldsymbol{r}_i^{\mathrm{old}} \approx \sqrt{i} \Delta \hat{r}_i$$

where $\hat{r}_i$ is indicating a unit vector. From this we get for a single successful double-bridging move

$$\langle \Delta \boldsymbol{R}_{\mathrm{cm}}^2 \rangle_n \approx \frac{1}{N^2} \sum_{i,j=n+1}^{N} \sqrt{ij} \langle \Delta \hat{r}_i \cdot \Delta \hat{r}_j \rangle .$$

When we approximate $\Delta \hat{r}_i$ and $\Delta \hat{r}_j$ as being uncorrelated this reduces to

$$\langle \Delta \boldsymbol{R}_{\mathrm{cm}}^2 \rangle_n \approx \frac{\langle \Delta \hat{r}_i^2 \rangle}{2} \left(1 - \frac{n(n+1)}{N^2} \right) .$$

Averaging this finally over the position of the attacking monomer yields

$$\langle \Delta \boldsymbol{R}_{\mathrm{cm}}^2 \rangle = \Delta R_0^2 \left(1 - \frac{a_1}{N} + \frac{a_2}{N^2} \right) . \tag{8}$$

The center of mass of the polymers therefore will perform a random walk with an average step length which increases up to a saturation value when the chain length N goes to infinity. In a similar fashion one can calculate the amount of decorrelation of the unit

vector along the end-to-end vector of a chain in a single successful double-bridging move and arrive at

$$\Delta\phi(t) = -c_0 \left(1 - \frac{c_1}{N}\right) \ . \tag{9}$$

This behavior gives rise to an increase of the measured autocorrelation time for the end-to-end vector with decreasing chain length. Qualitatively this is observed in the simulations[20] as can be seen in Fig. 4.

$$\tau_{\rm N} = \tau_\infty (1 + \frac{c_1}{N}) \ . \tag{10}$$

When one performs an exponential fit to the short time decay observable in figure 4 and

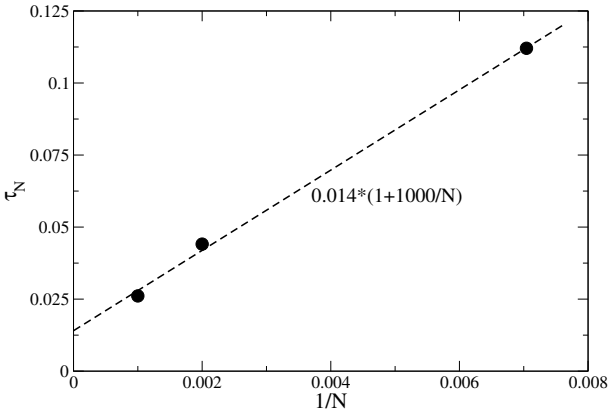

Figure 5. Autocorrelation time for the end-to-end vector reorientation in figure 4 versus inverse chain length. The predicted scaling is nicely compatible with the data.

then plots the simulation time per chain (note that for Fig. 4 the number of monomers was fixed) as a function of inverse chain length, the scaling of equ. (10) is clearly observed (see Fig. 5).

We already commented on the fact that the connectivity changing algorithms are especially efficient in decorrelating large scale structure in the melt. They are typically augmented by local moves and reptation moves to equilibrate the local structure. Before we turn to a detailed discussion of the local relaxation and the energetics involved in this for a chemically realistic polymer melt we want to mention an alternative method for overcoming the entropic slowing down in a polymer melt. This method has so far been tested on the structural relaxation of a collapsed polymer globule where the connectivity of the chains and the high density inside the globule lead to a dramatic increase in the structural relaxation time of the globule. The idea of this algorithm[24] is to turn part of the monomers into ghost particles (alternatively one can think of removing some particles into the fourth dimension similar to desorbing and readsorbing particles from a two dimensional film into the third dimension) and forcing them back into the three dimensional structure by applying

an external field. One can formulate this algorithm in the context of a parallel tempering simulation of an extended system Hamiltonian

$$H = H_0 + \sum_{i=1}^{N_{\rm part}} h x_4(i)\,,$$

where H_0 is the real Hamiltonian of the model system, the external field h is set to different values labeling the replicas of the real system, and the fourth coordinate $x_4(i)$ of monomer i reduced to being either 0 or 1. The partition function of the extended ensemble in a parallel tempering simulation therefore reads

$$Z = \prod_h \sum_{\{c\}} \exp\left\{ -\frac{H_0 + \sum_{i=1}^{N_{\rm part}} h x_4(i)}{k_{\rm B}T} \right\}\,, \tag{11}$$

where $\sum_{\{c\}}$ indicates a sum over all configurations at fixed h. The external field h determines the average number of ghost particles. For $h = 0$ half the particles are ghost particles and for $h \to \infty$ all particles are back in the original threedimensional system. In this way excluded volume as well as connectivity constraints are partially removed. In the application to the equilibration of a collapsed polymer globule it became possible for the first time to identify a liquid to solid transition in the globular phase. In principle, this scheme is applicable to coarse-grained and chemically realistic continuum models as well, although its efficiency will depend on whether packing and connectivity or local energetics are the dominating factor for the slow-down of relaxation processes. The latter will be discussed in detail in the next section.

3 Local Relaxation in Polymer Melts

In the last section we dealt with the chain length dependence of the longest relaxation time in a polymer melt and with advanced MC algorithms to overcome this slowing down. We did not dwell on the prefactor $\tau_{\rm mes}(T)$ and its temperature dependence which typically spans 14 orders of magnitude when we study a glass forming polymer melt above T_g. In order to understand the physical origin of this slowing down and the relative importance of energetic effects (intramolecular dihedral potential) versus packing effects (which are entropic in origin) one has to use chemically realistic modeling. We will present in this section MD simulations of a random copolymer of 50 % trans 1,4-PB, 40 % cis 1,4-PB and 10% vinyl groups. This polymer was synthesized with an average molecular weight corresponding to about 30 repeat units and characterized to possess the above chemical micro structure[13]. We have 40 chains of 30 repeat units in our simulation box and we will be using a united atom model for the CH, CH_2 and CH_3 groups. With a total of about 5000 united atoms, these systems can be simulated today over a time range of several 100 ns (about 2 ns of real time trajectory per day on a single processor).

The ability of the simulation to quantitatively reproduce experimental data on relaxation processes in polymer melts strongly rests on the implementation of the correct force fields for the dihedral angles. These typically possess barriers separating the isomeric states as was discussed in the section on the force field, and it is by correlated jumps over these barriers[25,5,6] that the local relaxation processes come about. The frequency of these

jumps is exponentially sensitive to the height of the barriers. In order to be able to make a parameter free quantitative comparison with experiment one therefore needs to carefully determine this part of the force field[13], which is done through high-level quantum chemistry calculations. The validation of this force field then proceeds through comparison with experiment.

3.1 NMR Experiments

An experimental technique which is very sensitive to the local dihedral barriers is C^{13} NMR spin lattice relaxation time measurements.

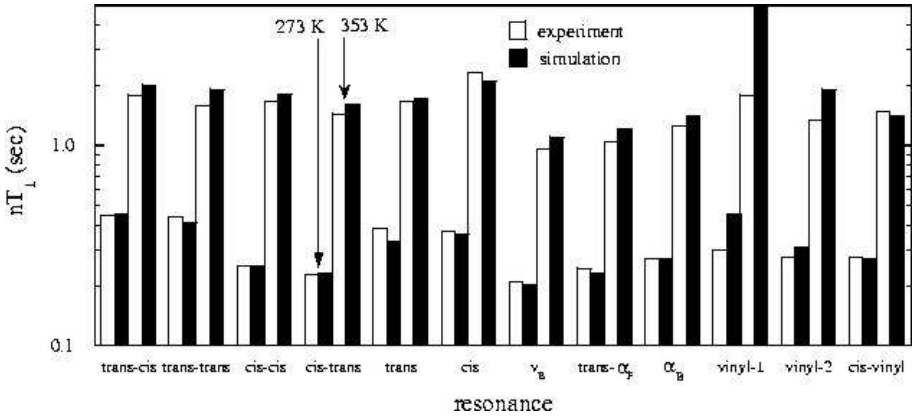

Figure 6. Comparison of the spin lattice relaxation times determined from MD simulations and experiment for two different temperatures. The figure shows data for 12 different resonances (cis-cis for example indicates an sp^2 carbon in a cis group next to another cis group, trans an sp^3 carbon of a trans group)

For polymers like PB this technique observes the reorientational motion of the CH bonds as quantified through the second Legendre polynomial of the CH bond orientational autocorrelation function. It is sensitive to the local chemical environment of the relaxing bond giving rise to 12 different resonances which can be identified[26]. A CH bond at the sp^2 carbon of the double bond in a cis group next to a trans group (see Fig. 1)relaxes differently from one next to another cis group and differently from the ones in a trans group and differently from the CH bonds at a sp^3 carbon. The vinyl group alone gives rise to six different resonances.

In a computer simulation one measures the CH vector autocorrelation function and determines the second Legendre polynomial according to

$$P_2^{\mathrm{CH}}(t) = \frac{1}{2}\left(3\left\langle\left[\boldsymbol{e}_{\mathrm{CH}}(t)\cdot\boldsymbol{e}_{\mathrm{CH}}(0)\right]^2\right\rangle - 1\right) \tag{12}$$

From this function one obtains the spectral density by Fourier transformation

$$J(\omega) = \frac{1}{2}\int_{-\infty}^{\infty} P_2^{\mathrm{CH}}(t)\mathrm{e}^{i\omega t}dt\ . \tag{13}$$

The spin-lattice relaxation time finally is given by evaluating the spectral density at the Larmor frequencies of carbon and hydrogen atoms

$$\frac{1}{nT_1} = K\ [J(\omega_{\mathrm{H}} - \omega_{\mathrm{C}}) + 3J(\omega_{\mathrm{C}}) + 6J(\omega_{\mathrm{H}} + \omega_{\mathrm{C}})] \tag{14}$$

where ω_H, ω_C are Larmor frequencies, K is a constant depending on the hybridization of the nucleus and n is the number of hydrogen atoms attached to the carbon atom under study.

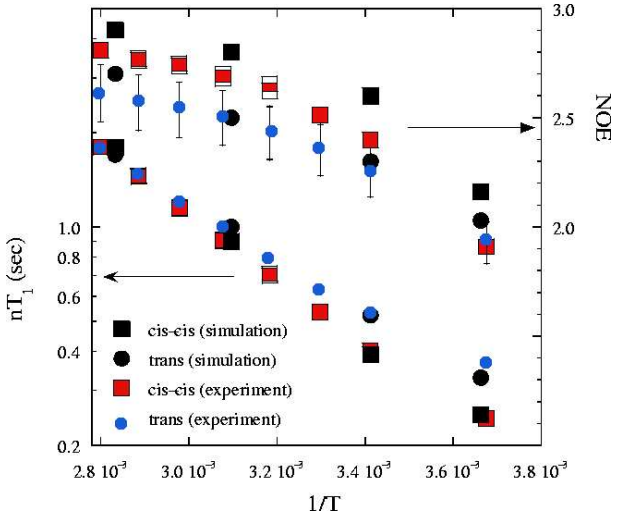

Figure 7. Comparison of the spin lattice relaxation times determined from MD simulations and experiment for the cis-cis (sp^2) and the trans (sp^3) resonance as a function of inverse temperature. Also shown are results for the nuclear Overhauser enhancement which is a measure of the non-exponentiality of the observed relaxation

To be able to evaluate this function from a stored trajectory of a simulation of a united atom model, we have to reinsert hydrogen atoms into the system. This is done using the information on equilibrium ($T = 0$) bond lengths and angles which allows the determination of the hydrogen positions from the positions of the carbon backbone atoms (united atoms) alone. In Fig 6 we show a comparison between experiment and simulation for the 12 resolvable resonances for two different temperatures. As one can see, there is a very good agreement (better than within 10%) between simulation and experiment for all but one resonance. The one that is not reproduced is a rigid body rotation of the side group which does not lead to a conformation relaxation and which we therefore did not try to match more accurately. The temperature dependence of the spin lattice relaxation time for two resonances can be seen in Fig. 7

The spin lattice relaxation time decreases when the autocorrelation time for the observed relaxation increases. For high temperatures, where the nuclear Overhauser enhancement is still close to three[27], the spin lattice relaxation time traces the temperature dependence of the autocorrelation time of the torsional transitions and the agreement between simulation and experiment is a quantitative validation of the torsional force field[26].

From comparing to the observed torsional autocorrelation function in the simulation one can learn that this identification of the physical motion seen in the NMR experiment breaks down below about 300 K. In Fig. 8 we compare different measures of the local orientational

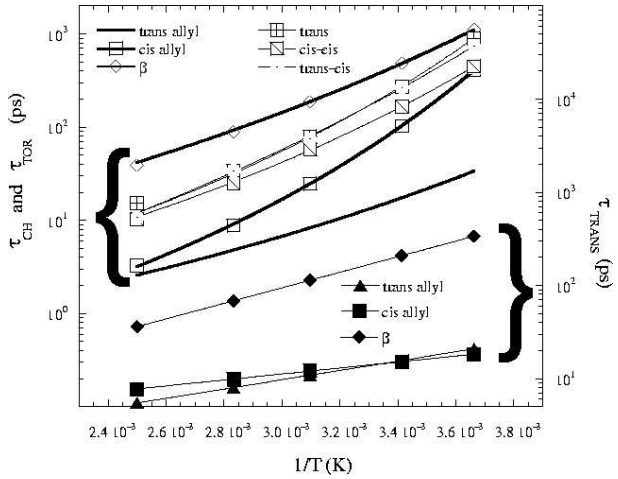

Figure 8. Temperature dependence of several measures of the local orientational mobility of the chain. The lower set of curves pertaining to the right abscissa shows the mean time between torsional transitions for the three relevant torsional potentials along the chain. The upper two sets of curves give the integrated autocorrelation time for the second Legendre polynomial of the CH vector orientation, τ_{CH}, and the integrated autocorrelation time for the torsion angle autocorrelation function, τ_{TOR}.

mobility of the chains. The most basic one is the mean time between torsional transitions which we determined with a time resolution of 1 ps along the simulated trajectory. This time scale shows an Arrhenius temperature dependence. It is different for the three relevant torsion potentials along the chain, the allyl bonds next to a cis or trans double bond and the β bond at the connection between two PB monomers. All these time scales, however, simply follow an Arrhenius law with their energetic dihedral barrier as activation energy in the observed temperature range, so that there are no packing effects observable on the dihedral dynamics in this range. Contrary to the mean time between torsional transitions, the autocorrelation time for the torsions (thick lines in Fig. 8) defined as the time integral of the following correlation function

$$f(t) = \frac{\langle \cos(\phi(t))\cos(\phi(0))\rangle - \langle \cos(\phi(0))\rangle^2}{\langle \cos(\phi(0))^2\rangle - \langle \cos(\phi(0))\rangle^2} \,, \tag{15}$$

increases in a Vogel-Fulcher like manner. This shows the growing importance of back-jump correlations for the torsional transitions: a torsional transition which occurs with its Arrhenius rate is immediately reversed with an increasing probability upon reducing the temperature, thus leading to no decorrelation of the torsional angle. The final set of curves denoted by their resonance name in the figure legend gives the autocorrelation time of the second Legendre polynomial for the CH vectors, i.e., the time integral of $P_2(t)$ in equ. (12). These time scales pick up contributions from different torsions adjacent to the carbon

atom under study and lie intermediate to the autocorrelation functions of these torsions. Another technique which is taken as a measure of local relaxation processes in polymer melts is dielectric relaxation which we will discuss in the following.

3.2 Dielectric Relaxation Experiments

Dielectric relaxation measurements couple to the dynamics of the dipole moment of the sample. The dielectric permittivity is the Fourier-Laplace transform of the dipole moment autocorrelation function.

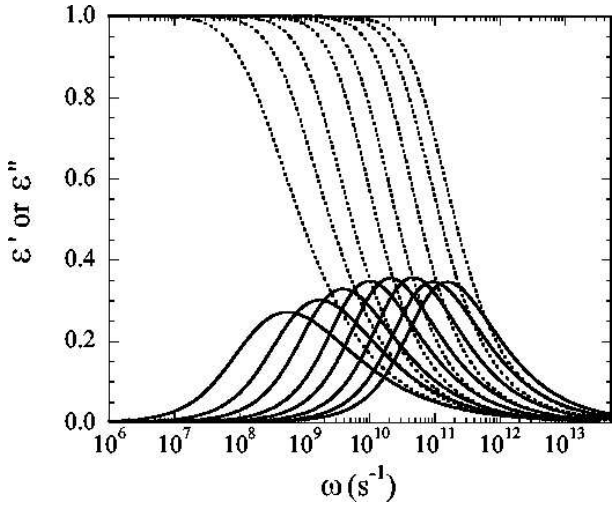

Figure 9. Real and imaginary part of the dielectric permittivity as a function of frequency.

$$\frac{\epsilon' + i\epsilon''}{\Delta\epsilon} = 1 - i\omega \int_0^\infty \Phi(t) e^{-i\omega t} dt \tag{16}$$

with $\Phi(t)$ defined as

$$\Phi(t) = \frac{\langle \boldsymbol{M}(t) \cdot \boldsymbol{M}(0) \rangle}{\langle \boldsymbol{M}(0) \cdot \boldsymbol{M}(0) \rangle} \, .$$

Furthermore we have used the following relation for the dielectric relaxation strength

$$\Delta\epsilon = \epsilon_r - \epsilon_u = \left(\frac{\epsilon_u + 2}{3} \right)^2 \frac{3\epsilon_r}{2\epsilon_r + \epsilon_u} \frac{\langle M(0)^2 \rangle}{3V\epsilon_0 k_B T}$$

where ϵ_u and ϵ_r are the unrelaxed and relaxed dielectric constants of the material, respectively. The dipole moment of the box is the sum of local dipole moments along the chains so that $\Phi(t)$ in principle contains correlations between all local dipole moments, intramolecular and inter-molecular. A comparison with chemically realistic MD simulations can help to identify the independently relaxing dipoles observed in the experiment.

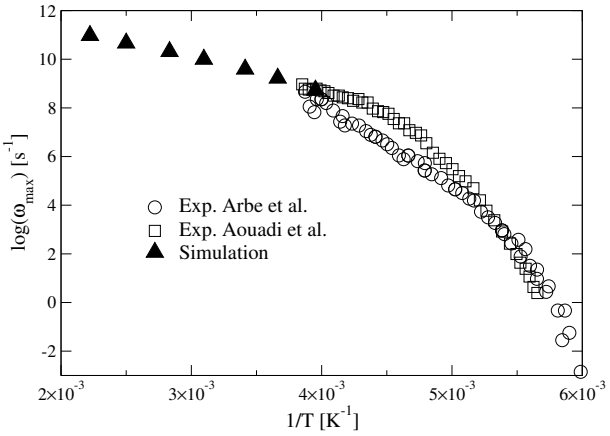

Figure 10. Position of the peak in the dielectric loss as a function of temperature for the simulation (filled triangles) and two sets of experimental data (open circles[28] and open squares[29]). The experiments show some scatter, but the in the overlap temperature regime experiment and simulation agree.

For PB the dipole moments are located on the vinyl side group and the cis group. The partial charges, however, are small and that was the reason we did not include Coulomb forces into our MD simulation. Consequently, there can be no correlations due to the local dipole moment occurring in our simulation trajectory. We then have to see, how well our results for the dielectric permittivity agree with the experiments[27]. To this end we reinsert partial charges into the simulated trajectory. We know that we have to find

$$\langle M^2(0)\rangle = N_{\mathrm{chains}}\langle M^2_{\mathrm{chain}}(0)\rangle$$

and we also find that the autocorrelation function of the box dipole moment can be calculated through the autocorrelation function of the chain dipole moment

$$\Phi(t) = \Phi_{\mathrm{chain}}(t)$$

which has a 40 times better statistics. In Fig. 9 we show the real and imaginary part of the dielectric permittivity as obtained from the simulation. The frequencies of maximum loss can now be compared with experimental results Experimentally the maximum loss frequency is typically measured for lower temperatures[28,29] to study the temperature dependence of the structural glass transition or α process. Two sets of experiments in the literature show some discrepancies in an intermediate temperature range but agree with each other and with our simulation data at higher temperatures where we have an overlap temperature window between simulation and experiment. From this we can conclude, that also in the experiment one sees no correlations between the dipole moments of different chains. When we furthermore compare the time scale given by the maximum loss frequency with the time scales of the Rouse modes for our chains we can obtain from the simulation, we can say that the dielectric measurements on PB see the relaxation of a chain segment of about 6 backbone carbons, which is exactly the length of a statistical segment of the chains.

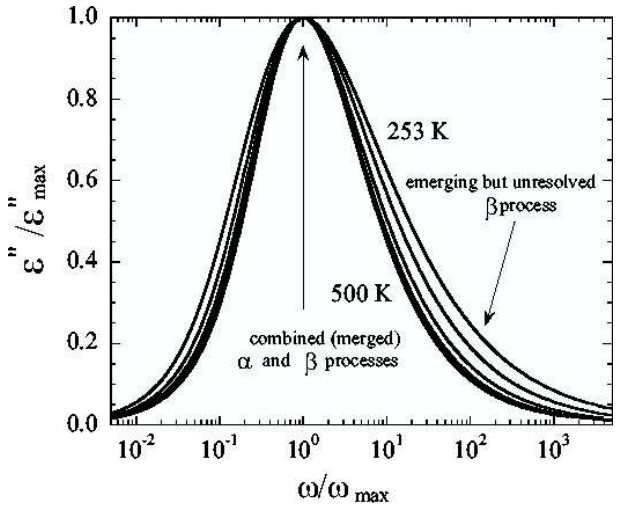

Figure 11. Time temperature superposition applied to the dielectric loss data obtained from the computer simulation in a temperature range from 500 K down to 253 K.

Many glass-forming materials show two distinct relaxation processes at low temperatures in their dielectric spectrum, called the α-process - which shows a Vogel-Fulcher-Tamman temperature dependence - and the β-process - which shows an Arrhenius temperature dependence. In the temperature regime accessible to our MD simulations so far we are actually observing the so-called combined $\alpha - \beta$ process, i.e., there has been no separation of time scales yet between the two processes which can be observed at lower temperatures. For a single type of relaxation mechanism underlying the dielectric spectrum we should be able to see time-temperature superposition if we scale the dielectric loss data in Fig. 9 by the peak position and peak height, respectively, which is shown in Fig. 11.

Our results in Fig. 11 show that the time temperature superposition is only borne out for temperatures above 300 K. Below this temperature the scaling breaks down, indicating a change in the molecular motion mechanisms underlying the dielectric data observed. We interpret this as the emergence of the β process which becomes clearly resolvable as an independent feature in the loss spectrum only at lower temperatures.

Let us now come to the question of increasing heterogeneity in the local mobilities upon decreasing the temperature. We have already identified a tendency for immediate back jumps after one torsional transition as the reason for the different temperature dependencies of the mean waiting time between torsional transitions $\langle t_{\rm wait} \rangle$ and the torsional autocorrelation time. In a homogeneous system, where every chemically identical torsion shows identical dynamics on the time scales of observation, the probability distribution of waiting times should be Poissonian. As we can see in Fig. 12 which shows the waiting time distribution for the 10th jump to occur for temperatures $T = 500$ K, 450 K, 400 K, 353 K, 323 K, 293 K, 273 K and 253 K, at high temperatures the curves approach the Poisson distribution indicated by the fat line in the figure. At lower temperatures two features emerge. There is an increasing probability of very short waiting times which captures the increasing amount of direct back jumps for the dihedral transitions. Furthermore the distribution

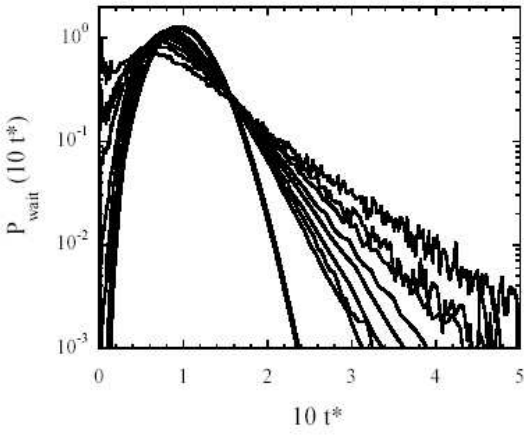

Figure 12. Distribution of waiting times for a total of 10 torsional transitions per dihedral degree of freedom to occur plotted versus 10 times $t/\langle t_{\rm wait}$.

develops a fat tail toward very long waiting times indicating the increasing heterogeneity between the different torsion angles. For high temperatures this heterogeneity will also show up on the distribution for the average waiting time until the next jump occurs, but on the scale of 10 jumps the heterogeneity at high temperatures has been smeared out: slow angles have had time to become fast and vice versa. At low temperatures this homogenization time becomes much longer than the time scales observed for the jump distribution and the two extremes of the mobility distribution show up clearly. When we characterize the distribution of waiting times for several values of n, the number of transitions observed, by their normalized dispersion

$$D(n,T) = \sigma^2(n,T)/n$$

this means that at fixed temperature $D(n,T)$ becomes smaller with increasing n approaching the Poisson limit of $1/n$. For fixed n, $D(n,t)$ increases dramatically with decreasing temperature due to the fat tails developing in the waiting time distribution. We can define a measure for the homogenization time of the dihedral mobility by determining the number of jumps $n^*(T)$ (this will be a real value determined by interpolation) after which D(n,T) reaches a fixed value, for example $D(n^*,T) = 1$. This corresponds to a time scale $t^*(T) = n^*(T)\langle t_{\rm wait}\rangle(T)$. The temperature dependence of this time scale is compared in Fig. 13 with that of the average waiting time and the torsional autocorrelation time. It is clear from this comparison that the torsional autocorrelation time is sensitive to this homogenization process of the torsional mobilities and that the slowing down of this homogenization leads to the stronger than Arrhenius-like increase in relaxation time as compared to the average waiting time between transitions.

3.3 Changing the Model Hamiltonian

So far we have presented MD simulations of a chemically realistic united atom model for PB employing a carefully validated quantum chemistry based force-field. For the following

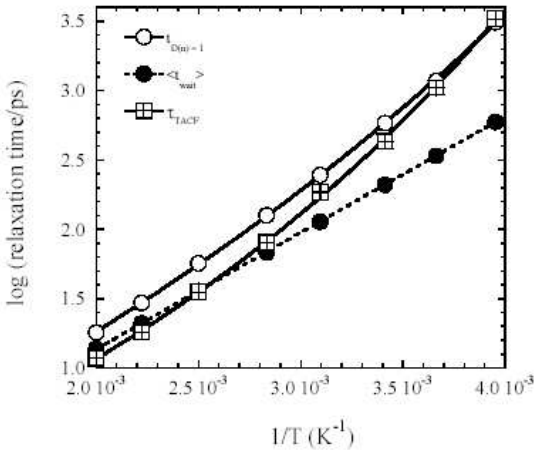

Figure 13. Homogenization time scale for the dihedral mobilities compared to the average waiting time and the dihedral angle autocorrelation time.

study we will slightly modify the chemically realistic model to one without vinyl side groups, i.e. it will be random copolymer of 55 % trans 1,4-PB and 45 % cis 1,4-PB. We will again have 40 chains of now 29 repeat units (115 backbone carbons) in our simulation box and will be using the same united atom force field. We have seen that we can understand the physics of local relaxation processes observed in NMR and dielectric experiments with an understanding of the dihedral potentials along the chain. But how important is this enthalpic effect compared to the entropic packing effects? To resolve this question is a necessary prerequisite to understanding the glass transition in real polymer melts as well as the dynamic response of polymer blends. To bring out the effects of the torsional barriers on the local dynamics of the atoms most dramatically, we use the ability of the simulation approach to modify parts of the force field selectively. We will compare the results from the chemically realistic chain (CRC) model simulations to those for a freely rotating chain (FRC) version of this CRC model, where we switch off all torsion potentials[30]. Let us first show that in the case of PB this has no effect on the static structure of the melt.

When we discuss the static structure of an amorphous polymer melt we always have to take into account two different measures of that structure. One of these is the chain structure as described by the single chain structure factor

$$S(q) = \langle \frac{1}{N} \sum_{i=1}^{N} e^{i\boldsymbol{q}\cdot\boldsymbol{r}_n} \rangle \tag{17}$$

where the average is meant to include a spherical and a thermal average. This function is shown in Fig. 14 for $T = 240, 273$ and 353 K for the CRC model and for 273 K for the FRC model. The behavior for small momentum transfers agrees well with the Debye function $f_D(x) = \frac{2}{x^4}(e^{-x^2} + x^2 - 1)$ where $x = qR_g$, which describes the scattering of a Gaussian coil. The obtained value for the radius of gyration agrees well with the directly measured value. The single chain structure factor shows no temperature dependence in the

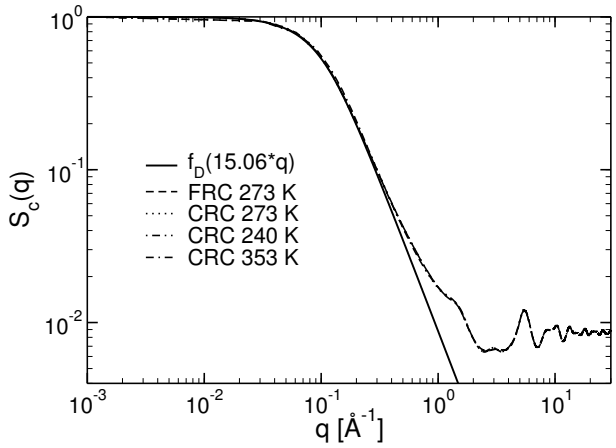

Figure 14. Single chain structure factor for the CRC model at different temperatures indicated in the legend and for the FRC model at 273 K. Also included is the Debye function which fits the behavior for small momentum transfers.

depicted temperature range and agrees perfectly between the FRC and CRC models. This is a peculiarity of PB since for this polymer all minima in the different dihedral potentials are iso-energetic, which also explains the lack of temperature dependence of the single chain structure factor of the CRC model.

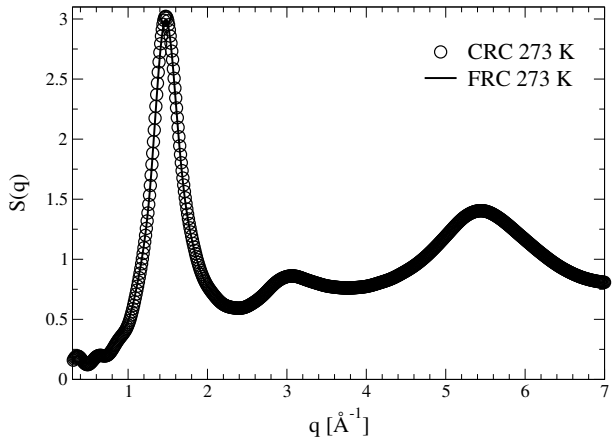

Figure 15. Melt structure factor for PB as obtained from simulations of the CRC model and the FRC model at 273 K.

The other quantity characterizing the melt structure is the liquid structure factor. This is shown over a wide momentum transfer range in Fig.15 at 273 K. For the calculation

we have used the united atoms as scattering centers of equal scattering strength, calculating in this way the structure of the actual simulated systems. A quantitative comparison to the structure factor of PB would be improved by reinserting the hydrogen atoms into their mechanical equilibrium positions[6] and explicitly using the scattering lengths of the carbon and hydrogen atoms in the system. It is gratifying, that even so the position of the amorphous halo at $q = 1.47$ Å^{-1} agrees nicely with the experimental results[31] and also the behavior at higher momentum transfers is comparable. We have performed both sets of simulations at the equilibrium density of the CRC model and this result shows that under these conditions the liquid structure is the same in both models.

In the preceding paragraphs we have shown that we have two models at hand which show the same static structure (packing) on the level of the two-body correlation functions. Do they have the same dynamics? The high temperature behavior of the CRC model

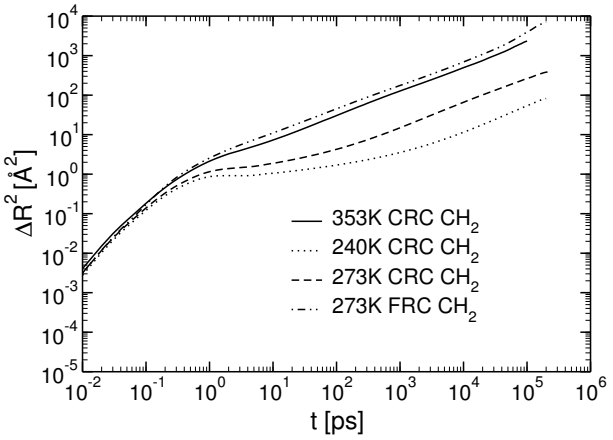

Figure 16. Mean square displacements of the sp^3 carbons along the chain back-bone as a function of time for several temperatures for the CRC model and for $T = 273$ K for the FRC model.

(curve at $T = 353$ K in Fig. 16) and the behavior of the FRC model agree. One observes a crossover from short time ballistic and vibrational motion to a subdiffusive Rouse-like regime determined by the connectivity of the chains. For the CRC model at 273 K, however, one observes a plateau intervening between the short time motion and the Rouse-like regime and this plateau becomes more pronounced upon lowering the temperature to 240 K. It starts at around $t = 1$ ps and extends almost to 100 ps for 240 K. This slowing down is not due to packing effects but obviously due to the presence of intramolecular barriers against dihedral rotation. On the time scale of 1 ps the fast vibrational dynamics of the bond angles and torsion angles is damped out and this time scale is not strongly dependent on temperature. The mean time between torsional transitions, however, as we have seen increases in an Arrhenius-like fashion with decreasing temperature. Consequently we are observing a separation of time scales between the vibrational dynamics and the relaxational dynamics governed by the torsional transitions. At 240 K the mean waiting time between torsional transitions has reached about 100 ps and this is exactly the time scale

of the break-up of the plateau. For shorter times the mean-squared displacement curves only pick up contributions from the fast-moving torsions in the waiting time distribution and upon lowering the temperature these become fewer and fewer (at a fixed time). This result extends to lower temperatures showing that the glass transition in PB is strongly influenced by enthalpic effects and not given by the intermolecular packing[32] alone. In the next section we will now focus on the large scale dynamics in chemically realistic polymer melts.

4 Large Scale Relaxation as Observable in Neutron Scattering Experiments

The comparison between neutron scattering experiments and MD simulations can be done on several length and time scales. Comparing to incoherent scattering as for example measured in time of flight experiments[33–35] one focuses on small length scales (momentum transfers of about one inverse Ångstrœm) and time scales below 1 ns and the motion of individual atoms. This yields complementary information to the one obtained from the comparison with NMR experiments.

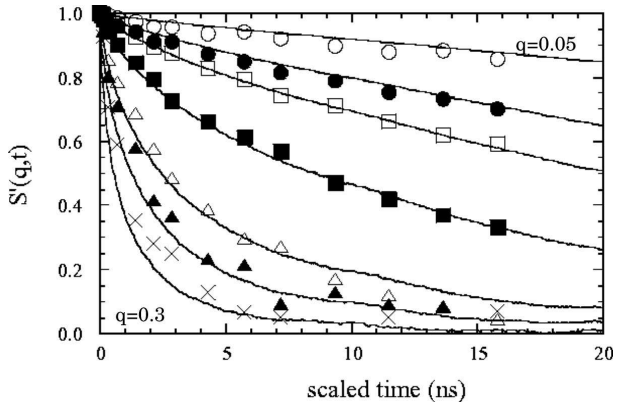

Figure 17. Single chain coherent intermediate scattering function for PB at 353 K compared between experiment and simulation. Simulation times are scaled by a factor of 0.8 to account for a difference in center of mass diffusion coefficient.

On larger length and time scales it is a challenge to reproduce in the simulations the dynamics of a single chain in the melt as observed in neutron spin echo (NSE) experiments[36]. These experiments measure the configurational relaxation of a polymer chain on varying length scales in form of the intermediate coherent scattering function of the chain

$$S'(q,t) = S(q,t)/S(q,0) = \frac{\left\langle \sum_{n,m} \mathrm{e}^{\mathrm{i}\boldsymbol{q}\cdot(\boldsymbol{r}_n(t)-\boldsymbol{r}_m(0))} \right\rangle}{\left\langle \sum_{n,m} \mathrm{e}^{\mathrm{i}\boldsymbol{q}\cdot(\boldsymbol{r}_n(0)-\boldsymbol{r}_m(0))} \right\rangle} \,. \tag{18}$$

Here the sums run over all atoms of the same chain, so one imagines an experiment where one has a few deuterated chains in a protonated matrix, giving rise to strong coherent scattering between the atoms of one single chain.

This quantity is easily calculated from the computer simulation and Fig. 17 shows a comparison[13] of the results from the simulation (lines) to the experimental data (symbols) for a momentum transfer range of $q = 0.05$ Å^{-1} to $q = 0.3$ Å^{-1}. It turned out that there is an overall difference in center of mass diffusivity of about 20 % between simulation and experiment similar to earlier experience[37], so for the figure the experimental time points are rescaled by a factor 0.8. This makes the whole set of scattering curves, measuring the configurational relaxation of the polymer chain on different length scales superimpose.

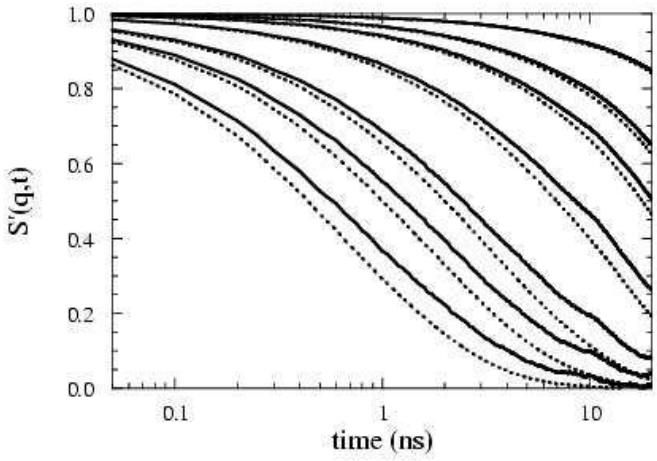

Figure 18. Single chain coherent intermediate scattering function for PB at 353 K (full lines) compared to the Rouse model prediction (dashed lines).

Polymer melt relaxation on these length and time scales and for chains below the entanglement molecular weight, as in our case, is typically analyzed within the Rouse model. The equation of motion for this chain of phantom beads

$$\begin{aligned} \zeta d\boldsymbol{r}_n &= \frac{3k_{\mathrm{B}}T}{\sigma^2}\left(\boldsymbol{r}_{n+1} - 2\boldsymbol{r}_n + \boldsymbol{r}_{n-1}\right)dt + d\boldsymbol{W}_n(t) \\ \langle dW_{n\alpha}(t)\rangle &= 0 \\ \langle dW_{n\alpha}(t) dW_{m\beta}(t')\rangle &= \delta_{nm}\delta_{\alpha\beta}\delta(t-t')2\zeta k_{\mathrm{B}}T dt \end{aligned} \tag{19}$$

can be solved analytically and there is a closed expression for the single chain coherent intermediate scattering function

$$\begin{aligned} S(q,t) = \frac{1}{N}\exp\left\{-q^2Dt\right\}\sum_{n,m=1}^{N}\exp\Bigg\{-\frac{q^2\sigma^2}{6}|n-m| - \frac{2Nq^2\sigma^2}{3\pi^2} \\ \times \sum_{p=1}^{N}\cos\left(\frac{p\pi n}{N}\right)\cos\left(\frac{p\pi m}{N}\right)\left(1 - e^{-p^2 t/\tau_{\mathrm{R}}}\right)\Bigg\}\ . \end{aligned} \tag{20}$$

This function depends only on the length scale σ of the model and the segmental friction ζ entering the center of mass diffusion coefficient $D_{\mathrm{N}} = k_{\mathrm{B}}T/N\zeta$ and the longest relaxation time of the chain $\tau_{\mathrm{R}} = \zeta N^2\sigma^2/3\pi^2 k_{\mathrm{B}}T$. These quantities can be measured independently in the simulation so that we get a parameter free comparison to the prediction of the Rouse model (Fig. 18).

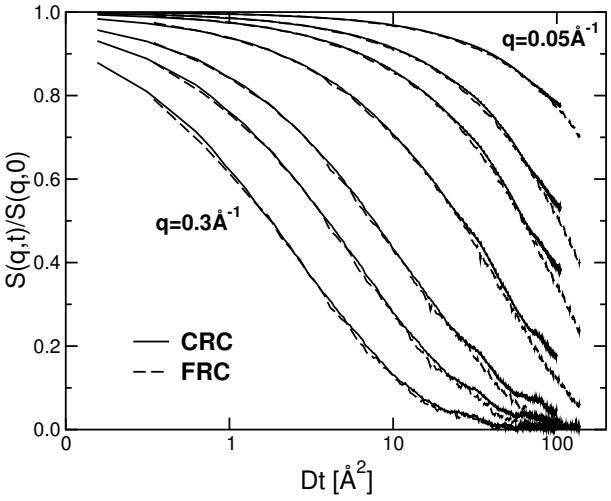

Figure 19. Comparison of the single chain coherent intermediate scattering function for the CRC (full lines) and FRC (dashed lines) models at 353 K. The difference in segmental friction is absorbed into a rescaling of the time axes by the chain center of mass diffusion coefficient.

The simulation data clearly show a stronger stretching compared to the Rouse model prediction, although there is an astonishingly good overall agreement considering the simple nature of the model. The differences are, however, significant and can be traced to the failure of the dynamic Gaussian assumption[38]

$$\langle \exp\{\mathrm{i}\boldsymbol{q}\cdot(\boldsymbol{r}_n(t)-\boldsymbol{r}_m(0))\}\rangle = \exp\left\{-\frac{q^2}{6}\langle(\boldsymbol{r}_n(t)-\boldsymbol{r}_m(0))^2\rangle\right\}$$

underlying the calculation of the scattering function. For the Rouse model this assumption is correct because it models the segmental motion as a Gaussian process, but in reality this assumption is not fulfilled due to interactions between a segment and its environment leading to non-Gaussian, heterogeneous mobility on the relevant time scales as we already discussed for the torsional dynamics.

As a final result on the large scale dynamics in polymer melts we can now come back to the question of universality. When we compare the results for the single chain intermediate scattering function of the CRC and FRC model[39] we expect them to be qualitatively the same. On the relevant time scales the difference in local dynamics observed in Fig. 16 gets absorbed into just one effective rate constant, the segmental friction ζ. One would therefore conclude that on these time and length scales the dynamics is the same after rescaling time scales for the difference in segmental friction and this is exactly what we find in Fig. 19.

5 Summary

In this contribution we have discussed on the one hand advanced MC methods for the equilibration of dense polymer systems, addressing slowing down due to entropic reasons, and chemically realistic MD simulations of 1,4-polybutadiene melts to exemplify the importance of local energetics for the understanding of relaxation processes in polymer melts. We have seen that modern connectivity altering MC algorithms are able to equilibrate the large-scale structure of polymer melts very efficiently, that they even increase in efficiency with increasing chain length. They can therefore provide starting configurations for MD simulations of chemically realistic polymer melts. These are targeted at understanding molecular structure and relaxations on small to intermediate length and time scales. They rely on carefully validated force fields which are able to quantitatively reproduce experimental data on well defined model systems. These force fields become available today thanks to a combination of experiments, high-level quantum chemistry calculations and simulations of simple model systems. Having established the ability of the simulation to reproduce available experimental data without any adjustable parameters one can then proceed to exploit the strong points of the simulation approach.

Where the range of thermodynamic parameters coverable in the simulation is often strongly limited, for those thermodynamic state points where a simulation in full equilibrium is possible one gets the complete information on the system under study down to every coordinate and momentum of every particle. This allows for measuring properties and correlations not available to experimental techniques, like for instance the distribution of waiting times between torsional transition, which are then instrumental in understanding and explaining effects of dynamic heterogeneity in polymer melts.

Another strong point of the simulation approach is its ability to selectively change parts of the model Hamiltonian. In this way we compared a chemically realistic model of PB with a freely rotating chain version of the same polymer and did not have to switch to a completely different polymer with some of the same properties like is unavoidable in experiments[40]. With this approach we could establish that identical structure on the two-body correlation function level (single chain and liquid structure factors) does not imply identical dynamics. Understanding the energetics of the dihedral potential is instrumental to understanding relaxation processes in polymer melts. These results also raise questions on the applicability of mode-coupling theory[41,42] to the glass transition in real polymer melts, because it relies on entropic packing effects as the cause for the glass transition.

Acknowledgments

It has been a pleasure to collaborate with G. D. Smith, S. Krushev, D. Bedrov and O. Borodin on the Molecular Dynamics simulations presented here. Obviously much of this work would not have been possible without the close collaboration with the following colleagues from the experiment side: M. D. Ediger, M. Monkenbusch, X. H. Qiu, D. Richter, L. Willner. The author acknowledges funding from the German Science Foundation under grant PA473/3-1,2 and BMBF under grant 03N6015.

References

1. K. Binder editor. *Monte Carlo and Molecular Dynamics Simulations in Polymer Science*. Oxford University Press, 1995.
2. M Doi and S. F. Edwards. *The Theory of Polymer Dynamics*. Oxford University Press, 1988.
3. S. C. Glotzer and W. Paul. Annu. Rev. Mater. Res. 32: 401, 2002.
4. R. Martoňák, W. Paul, and K. Binder. Phys. Rev. E, 57:2425, 1998.
5. G. D. Smith, Do Y. Yoon, W. Zhu, M. D. Ediger. *Macromolecules*, 27:5563, 1994.
6. W. Paul, Do Y. Yoon, and G. D. Smith, *J. Chem. Phys.*, 103:1702, 1995; W. Paul, G. D. Smith, and Do Y. Yoon, *Macromolecules*, 30:7772, 1997.
7. S. K. Nath, F. A. Escobedo, and J. J. de Pablo, *J. Chem. Phys.*, 108:9905, 1998; S. K. Nath, B. J Banaszak, and J. J. de Pablo, *J. Chem. Phys*, 114:3612, 2001; J. Budzien, C. Raphael, M. D. Ediger, J. J. de Pablo, *J. Chem. Phys.*, 116:8209, 2002.
8. M. Mondello, G. S. Grest, A. R. Garcia, and B. G Silbernagel, *J. Chem. Phys.*, 105:5208, 1996; M. Mondello and G. S. Grest *J. Chem. Phys.*, 106:9327, 1997; M. Mondello, G. S. Grest, E. B. Webb, and P. Peczak, *J. Chem. Phys.*, 109:798, 1998.
9. V. G. Mavrantzas and D. N. Theodorou, *Macromolecules*, 31:6310, 1998; V. A. Harmandaris, V. G. Mavrantzas, and D. N. Theodorou, *Macromolecules*, 31:7934, 1998; *ibid.*, 33:8062, 2000; V. G. Mavrantas and H. C. Öttinger, *Macromolecules*, 35:960, 2002.
10. M. Doxastakis, V. G. Mavrantzas, and D. N. Theodorou, *J. Chem. Phys.*, 115:11339, 2001; *ibid.*, 115:11352, 2001.
11. J. Colmenero, F. Alvarez, and A. Arbe, *Phys. Rev. E*, 65:041804, 2002.
12. K. Karatasos, F. Saija, and J.-P. Ryckaert, *Physica B*, 301:119, 2001; K. Karatasos and J.-P. Ryckaert, *Macromolecules*, 34:7232, 2001; K. Karatasos, J.-P. Ryckaert, R. Ricciardi, and F. Laupretre *Macromolecules*, 35:1451, 2002.
13. G. D. Smith and W. Paul. *J. Phys. Chem. A*, 102:1200, 1998; G. D. Smith, W. Paul, M. Monkenbusch, L. Willner, D. Richter, X. H. Qiu, and M. D. Ediger. *Macromolecules*, 32:8857, 1999.
14. R. Gee and R. H. Boyd, *J. Chem. Phys.*, 101:8028, 1994.
15. E. Kim, S. Misra, and W. L. Mattice, *Macromolecules*, 26:3424, 1993.
16. M. E. Tuckerman, B. J. Berne, and G. J. Martyna, *J. Chem. Phys.*, 97;1990, 1992; G. J. Martyna, M. E. Tuckerman, D. J. Tobias, and M. Klein, *Mol. Phys.*, 87:1117, 1996; A. Kopf, B. Dünweg, and W. Paul, *Comp. Phys. Commun.*, 101:1, 1997.
17. S. Geyler, T. Pakula, and J. Reiter, *J. Chem. Phys.*, 92:2676, 1990.
18. P. V. K. Pant and D. N. Theodorou, *Macromolecules*, 28:7224, 1995.
19. V. G. Mavrantzas, T. D. Boone, E. Zervopoulou, and D. N. Theodorou. Macromolecules, 32:5072, 1999; V. G. Mavrantzas and D. N. Theodorou, *Comput. Theor. Polym. Sci.*, 10:1 2000.
20. N. C. Karayiannis, V. G. Mavrantzas, and D. N. Theodorou, *Phys. Rev. Lett.*, 88:105503, 2002; N. C. Karayiannis, A. E. Giannousaki, V. G. Mavrantzas, and D. N. Theodorou, *J. Chem. Phys.*, 117:5465, 2002.
21. A. Uhlherr, V. G. Mavrantzas, M. Doxastakis, and D. N. Theodorou, *Macromolecules*, 34:8554, 2001; A. Uhlherr, M. Doxastakis, V. G. Mavrantzas, D. N. Theodorou, S. J. Leak, N. E. Adam, and P. E. Nyberg, *Europhys. Lett.*, 57:605, 2002.

22. M. G. Wu and M. W. Deem, *J. Chem. Phys.*, 111:6625, 1999.
23. D. N. Theodorou in *Bridging Time Scales: Molecular Simulations for the Next Decade*, P. Nielaba, M. Mareshal, and G. Ciccotti (Eds.), (Springer, Berlin, 2002), pp. 67-127.
24. W. Paul and M. Müller, *J. Chem. Phys.*, 115:630, 2001.
25. R. H. Boyd, R. H. Gee, J. Han, and Y. Jin. *J. Chem. Phys.*, 101:788, 1994.
26. G. D. Smith, O. Borodin, D. Bedrov, W. Paul, X. Qiu, and M. D. Ediger. *Macromolecules*, 34: 5192, 2001.
27. G. D. Smith, O. Borodin, and W. Paul. *J. Chem. Phys.*, 117:10350, 2002.
28. A. Arbe, D. Richter, J. Colmenero, and B. Farago. *Phys. Rev. E*, 54;3853, 1996.
29. A. Aouadi, M. J. Lebon, C. Dreyfus, B. Strube, W. Steffen, A. Patkowski, and M. R. Pick. *J. Phys. Condens. Matter*, 9:3803, 1997.
30. S. Krushev and W. Paul. *Phys. Rev. E*, 67:021806, 2003.
31. D. Richter, B. Frick, and B. Farago, *Phys. Rev. Lett.* 61:2465, 1988.
32. D. Bedrov, G. D. Smith, W. Paul, in preparation.
33. G. D. Smith, W. Paul, D. Y. Yoon, A. Zirkel, J. Hendricks, D. Richter, and H. Schober. *J. Chem. Phys.*, 107:4751, 1997.
34. K. Karatasos, F. Saija, J.-P. Ryckaert. *Physica B*, 301:119, 2001.
35. O. Ahumada, D. N. Theodorou, A. Triolo, V. Arrighi, C. Karatasos, and J.-P. Ryckaert. *Macromolecules*, 35:7110, 2002.
36. G. D. Smith, W. Paul, and D. Richter, *Chem. Phys.*, 261:61, 2000.
37. W. Paul, G. D. Smith, Do Y. Yoon, B. Farago, S. Rathgeber, A. Zirkel, L. Willner, and D. Richter. *Phys. Rev. Lett.*, 80:2346, 1998.
38. G. D. Smith, W. Paul, M. Monkenbusch, and D. Richer. *J. Chem. Phys.*, 114:4285, 2001.
39. S. Krushev, W. Paul, and G. D. Smith. *Macromolecules*, 35:4198, 2002.
40. A. Arbe, M. Monkenbusch, J. Stellbrink, D. Richter, B. Farago, K. Almdal, R. Faust. *Macromolecules*, 34:1281, 2001.
41. W. Götze and L. Sjögren. In *Transport Theory and Statistical Physics*. S. Yip and P. Nelson, eds., Marcel Decker, 1995, pp. 801.
42. S. H. Chong SH and M. Fuchs, *Phys. Rev. Lett.* 88:185702, 2002.